Spin determination of valence and inner hole states via the $^{208}Pb(\vec{d},t)^{207}Pb$ reaction at $E_d = 200$ MeV

H. Langevin-Joliot,[1] J. van de Wiele,[1] J. Guillot,[1] E. Gerlic,[3] L. H. Rosier,[1] A. Willis,[1] M. Morlet,[1] G. Duhamel-Chretien,[2] E. Tomasi-Gustafsson,[4] N. Blasi,[5] S. Micheletti,[5] and S. Y. van der Werf[6]

[1]*Institut de Physique Nucléaire, Institut National de Physique Nucléaire et de Physique des Particules, Centre National de la Recherche Scientifique, Boite Postale No. 1, 91406 Orsay, France*

[2]*Institut des Sciences Nucléaires, Institut National de Physique Nucléaire et de Physique des Particules, Centre National de la Recherche Scientifique, 53 avenue des Martyrs, 38026 Grenoble, France*

[3]*Institut de Physique Nucleaire, Institut National de Physique Nucléaire et de Physique des Particules, Centre National de la Recherche Scientifique, 43 boulevard du 11 Novembre, 69622 Lyon, Villeurbanne, France*

[4]*Laboratoire National Saturne, Centre d'Etudes Nucléaires Saclay, F-91191, Gif-sur-Yvette CEDEX, France*

[5]*Istituto Nazionale di Fisica Nucleare and University of Milan, Physics Department, via Celoria 16, 20133 Milan, Italy*

[6]*Kernfysisch Versneller Instituut, 9747 AA Groningen, The Netherlands*

(Received 29 December 1992)

Highly excited neutron hole states in ^{207}Pb have been studied via the $(\vec{d},t)$ reaction at $E_d = 200$ MeV using for the first time a polarized beam, with both vector and tensor components. The determination of overlapping neutron hole response functions takes advantage of the strong characteristic features of $j_- = l - \frac{1}{2}$ versus $j_+ = l + \frac{1}{2}$ level analyzing powers and of the good distorted wave Born approximation (DWBA) description of the reaction. A least-squares fit analysis of the σ, A_y, and A_{yy} angular distributions has allowed a determination of the high j transition spectroscopic factors contributing to the excitation energy bins up to $E_x = 14.5$ MeV. The results are compared in details with those relying only on l identification, previously obtained in the $1i_{13/2}$ and $1h_{9/2}$ valence state fragmentation up to $E_x = 6.7$ MeV and on the $1h_{11/2}$ strength up to ~ 10 MeV. Several previous conclusions are unambiguously confirmed, in particular, the attribution of the bump around $E_x = 8.2$ MeV to the $1h_{11/2}$ strength. In addition, the present experiment settles the attributions of several j_- versus j_+ valence groups and indicates that the $1h_{9/2}$ strength is spread up to ~ 10.8 MeV. The analysis performed up to $E_x = 14.5$ MeV gives the first determination of the $1h_{11/2}$ strength beyond the bump, and a first reliable evidence for the $1g_{7/2}$ strength, with the maximum around $E_x = 11$ MeV. $\sim 85\%$ of these inner hole state sum rules are exhausted in the studied excitation energy range. The spin-orbit splitting of $1h$ orbitals in ^{208}Pb deduced from the strength centroids is 5.2 MeV. The experimental strength distributions and the integral characteristics of the $1i_{13/2}$, $1h_{9/2}$, $1h_{11/2}$, and $1g_{7/2}$ hole states are compared with the results from different theoretical approaches, i.e., microscopic calculations of the fragmentation and phenomenological calculations of spectral functions in a modified mean field. The comparison reports on the sharing of the valence strengths between each quasihole level and the other fragments, characterized by their centroids and widths, and on the shape of the inner hole strength distributions, the centroids and spreading widths.

PACS number(s): 21.10.Pc, 24.70.+s, 27.80.+w

I. INTRODUCTION

Neutron pickup reactions on the doubly magic nucleus ^{208}Pb have been extensively studied with unpolarized beams. Detailed studies performed at rather low incident bombarding energies with good energy resolution have concentrated on the lower lying levels in ^{207}Pb [1,2]. Further experiments with the $(^3He,\alpha)$ reaction at 70 [3], 101 [4], 205 [5], and 283 MeV [6] have investigated much larger excitation energy ranges, up to $E_x = 28$, 25, 19, and 58 MeV, respectively. New groups of states have been observed below $E_x = 6.65$ MeV giving evidence for a large fragmentation of the $1i_{13/2}$, $2f_{7/2}$, and $1h_{9/2}$ valence hole strengths. Moreover, about 50% of the $1h_{11/2}$ inner hole strength has been located in a bump centered around $E_x = 8.5$ MeV. Narrow structures rising over that bump have been observed in the two experiments performed with the best energy resolution (typically 100 keV) [3,4]. Indications for the deeper $1g_{7/2}$ and $1g_{9/2}$ hole states are also discussed in Refs. [3–6].

The study of single hole response functions at high excitation energy is hampered by the large overlap of different subshells and by the physical background produced by reaction mechanisms other than direct pickup. The $(\vec{d},t)$ reaction performed at 200 MeV incident energy combines a strong selectivity for the population of high l hole states with new possibilities of spin determination via the measurement of vector and tensor analyzing powers. The few experiments with polarized beams via the $(\vec{p},d)$ or via the $(\vec{d},t)$ reactions on ^{208}Pb [7–12] bear only on the first valence levels. Significant discrepancies among the previous results concerning the valence state fragmentation as well as the need for unambiguous attributions of inner hole structures strongly motivate the

present work.

In a previous step of our investigation, we compared the $(\vec{d},t)$ reactions on ^{208}Pb induced by polarized deuteron beams with both vector and tensor components at two incident energies, $E_d=200$ and 360 MeV. The reaction at $E_d=200$ MeV was found to be much better suited as a spectroscopic tool. The analyzing powers allow a clear identification of pickup transitions, especially of $j_+=l+\frac{1}{2}$ versus $j_-=l-\frac{1}{2}$ transitions [13]. Moreover, the background of multistep reactions which appears at high excitation energy is comparatively smaller than at $E_d=360$ MeV.

The results obtained on the main valence levels, referred to further as the reference levels, have been presented in Ref. [13], together with the DWBA analysis. The present paper reports on the high lying valence states and on the hole states in the first inner shell of ^{207}Pb studied via the $(\vec{d},t)$ reaction at $E_d=200$ MeV.

The paper is organized as follows. The experimental procedure and the raw data are presented in Sec. II. The method used to analyze the data, starting with DWBA calculations, is described in Sec. III. The results of the analysis are presented in Sec. IV for the low and intermediate excitation energy regions and compared with other existing data. The fragmentation and spreading of the $1i_{13/2}$ and $1h_{9/2}$ valence states and of the $1h_{11/2}$ and $1g_{7/2}$ strengths in the first inner shell, presented in Sec. V, are compared with the available theoretical calculations. Section VI summarizes the results and conclusions.

II. EXPERIMENTAL PROCEDURE AND OVERALL FEATURES OF THE DATA

A. Experimental procedure

We have taken advantage of the polarized deuteron beam available at the Laboratoire National Saturne. The experimental setup used on the beam line SPES1 and the experimental procedure have been briefly described in Ref. [13].

The vector and tensor polarization parameters, periodically measured as described in Ref. [13], were stable within 2% and reached 90% and 85% of the corresponding maximum values. Enriched ^{208}Pb targets were used, with thickness of 16.7 mg/cm^2 and 50 mg/cm^2 respectively for the lower and higher excitation energy parts of the ^{207}Pb spectra. The corresponding energy resolutions were 120 and 140 keV. The time of flight selection of the tritons, together with the windows put on target position and angular variables, allowed a good rejection of spurious deuterons present at 3°.

The angular distributions were measured by 3° steps from 3° to 18° up to $E_x=9$ MeV, and from 3° to 12° up to $E_x=17$ MeV, using two field settings of the spectrometer. Higher excitation energies were only investigated at 3° (up to 21 MeV) and 6° (up to 27 MeV). The chosen horizontal and vertical angular acceptances were respectively 2.4° and 4.0°. ^{11}C impurity peaks have been eliminated from the spectra at 3°, 6°, and 9° with the help of a CH_2 target measurement.

B. Overall features of the experimental spectra

The ^{207}Pb spectra taken at 6° and 12°, averaged over the beam polarization, are shown in Fig. 1. In addition to the well known first levels, the spectra exhibit a large number of peaks corresponding to unresolved levels supposed to originate from valence hole fragmentation. Beyond a dip at $E_x=6.65$ MeV, narrow structures appear on a bump centered around $E_x=8.2$ MeV, very similar to those already attributed $1h_{11/2}$ in Refs. [3,4]. The spectra are then decreasing smoothly with no evidence for the expected $1g_{7/2}$ and $1g_{9/2}$ hole states. The narrow peak located at $E_x=20.6$ MeV corresponds to the $1h_{11/2}$ $T_>$ hole level previously identified in Refs. [14,15]. The decrease of the cross section toward the highest excitation energies is a feature expected for pure direct neutron pickup, as the allowed l transfers are decreasing from one major shell to the next inner one. The cross sections here measured at the highest excitation energies are however much too large in this respect, as discussed later on. This points to additional contributions from more complex reactions.

III. DWBA CALCULATIONS AND DATA ANALYSIS

The DWBA description of the reference level angular distributions has been discussed in detail in our previous paper [13]. Finite range calculations performed with S and D range functions in momentum space obtained with the Paris interaction have proved most successful when

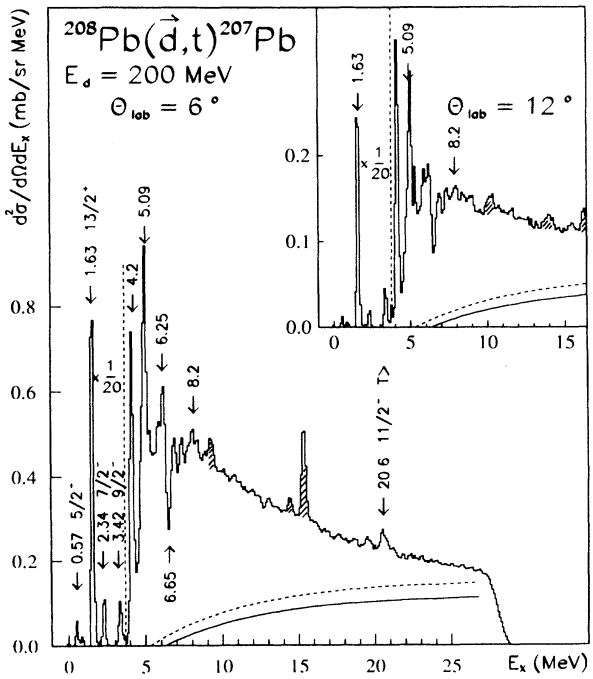

FIG. 1. Excitation energy spectra of the residual nucleus ^{207}Pb taken at $\theta_{lab}=6°$ and 12° via the $(\vec{d},t)$ reaction. Hatched areas correspond to oxygen and carbon impurity peaks. The solid line is the best estimate of the background and the dashed line shows the maximum background (see Sec. III).

used with the entrance and exit channel potentials D200B, T200B given in Table I of Ref. [13].

The experimental spectra do not exhibit other well resolved peaks than the reference levels. The analysis method described below has been used to determine, via a least-squares fit procedure, the spectroscopic factors of 2 or 3 different nlj transitions contributing to a same excitation energy bin.

Most generally, the relevant observables, functions of excitation energy and angle, are expressed as a linear sum of pickup contributions from different nlj transitions, labeled i and of a background contribution, as indicated in Eqs. (1):

$$\sigma^{\exp}=\sum_i C^2S_i\sigma_i^{\text{th}}+\sigma^b\ , \tag{1a}$$

$$\sigma^{\exp}A_y^{\exp}=\sum_i C^2S_i\sigma_i^{\text{th}}A_{y_i}^{\text{th}}+\sigma^bA_y^b\ , \tag{1b}$$

$$\sigma^{\exp}A_{yy}^{\exp}=\sum_i C^2S_i\sigma_i^{\text{th}}A_{yy_i}^{\text{th}}+\sigma^bA_{yy}^b\ . \tag{1c}$$

$\sigma^{\exp}$, $A_y^{\exp}$, $A_{yy}^{\exp}$ stand for the experimental cross section and analyzing powers at each angle and excitation energy and σ^b, A_y^b, A_{yy}^b are the background observables. C^2S_i is the spectroscopic factor of a nlj transition, while σ_i^{th}, $A_{y_i}^{\text{th}}$, $A_{yy_i}^{\text{th}}$ are input values calculated for the subshell i. The input values for valence transitions are derived from the DWBA predictions using correction factors to eliminate the residual discrepancies between the DWBA predictions and the reference level data (see Fig. 2). The required corrections are generally very small. Identical correction factors are adopted for transitions of same n and type (j_+ or j_-), such as $1i_{13/2}$, $1h_{11/2}$, for example, taking into account the similarity of the predicted angular distribution shapes [13].

A special point of interest for the DWBA analysis is the dependence of the form factor on the separation energy of a fragment which may be located several MeV away from the quasihole with the same nlj values. Preliminary attempts have indicated that form factors calculated for such levels with the standard well depth procedure would give angular distributions with a too small slope. A first set of calculations have been performed assuming no dependence of cross sections or analyzing powers with excitation energy for transitions of the same nlj. It has been suggested in Ref. [16] that a surface-peaked potential added to the core nucleus potential would be able to simulate the residual interactions responsible for the separation energy shift. The final calculations have been performed following this approach. Form factors have been obtained by solving an inhomogeneous equation including a phenomenological Woods-Saxon surface interaction located at $r=1.1A^{1/3}$ fm. The geometry of the volume part of the potential is that given in Ref. [19], as also used in Ref. [13]. For inner hole fragments, separation energies calculated in Ref. [19] were used to determine the potential depth.

A. Corrections for the background of multistep reactions

In the case of ejectiles heavier than the projectile the origin of the continuous physical background, which appears as a general feature in light ion reactions, is attributed to preequilibrium or multistep reactions. The main feature of such processes is the smooth dependence of angular distributions on ejectile energy and angle. The semiempirical parametrizations [17] describing fairly successfully many data on inclusive spectra cannot be used for the present experiment, due to the high incident deuteron energy and the forward angles involved. Under these conditions, we have estimated the cross sections and the analyzing powers of the background at the highest measured excitation energies by subtracting out the contributions of neutron pickup in all deep shells, using Eqs. (1).

Estimates of the contributions due to pickup were first made by using Hartree-Fock separation energies, calculated for the different subshells with the force Skyrme III [18]. A second set of separation energies shifted by 2 or 3 MeV following the predictions of Ref. [19] for the $1h_{11/2}$, $1g_{7/2}$, and $1g_{9/2}$ states was also used. Lorentzian shapes were adopted for all strength distributions. The widths of the deepest hole states were chosen typically 12 MeV while those of the $1g_{9/2}$ strength and the states in the

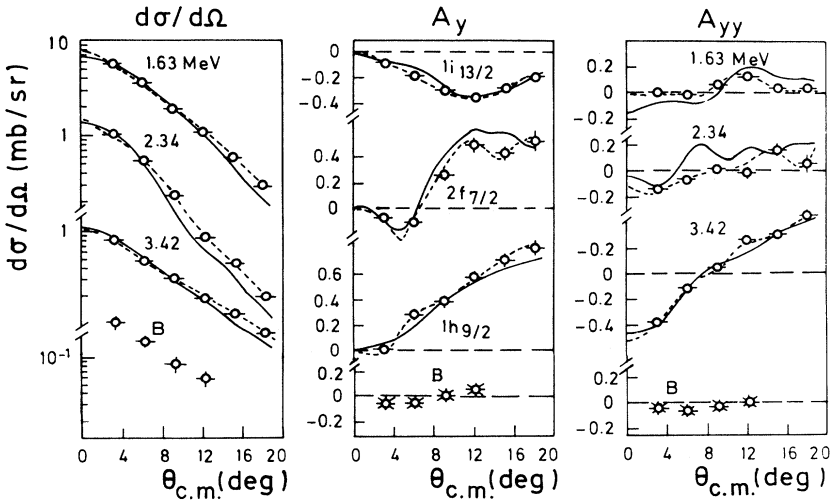

FIG. 2. Experimental angular distributions of the reference levels at $E_x=1.63$ MeV ($1i_{13/2}$), 2.34 MeV ($2f_{7/2}$), 3.42 MeV ($1h_{9/2}$), and of the background (B) at $E_x=16.5$ MeV. The dashed lines are empirical fits of the reference level angular distributions used for extracting correction factors applied to the DWBA predictions indicated as solid lines (see Sec. III).

first inner shell were varied from 3 to 7 MeV. The choice of narrow widths was however excluded, as it creates evident structures in the pickup spectra (of the unpolarized cross section as well as of the A_y or A_{yy} weighted cross section), in contradiction with the smooth behavior of the data.

The minimum background curve shown in Fig. 1 has been obtained beyond $E_x=18$ MeV after subtraction of the pickup contribution estimated for all inner shells. This curve is then smoothly extrapolated down to the energy axis. The upper curve represents a conservative estimation of the maximum background, obtained at $E_x=25$ MeV by only taking into account the shells deeper than $1g_{9/2}$.

The standard analysis has been performed with the minimum background choice. The same background shape is adopted in the small angular range spanned by the experiment. The experimental analyzing powers have also been corrected for the background contributions, taking into account the angular distributions of the background observables, as estimated at $E_x=16.5$ MeV (see Fig. 2) or adopting just background average vector and tensor analyzing powers for the whole angular range.

Taking into account the present limitations of our knowledge on the background observables, only the excitation energy region up to 14.5 MeV, clearly dominated by the pickup cross sections, has been considered in the following analysis.

IV. NEUTRON PICKUP TRANSITIONS UP TO $E_x=14.5$ MeV

The experimental spectra up to $E_x=14.5$ MeV have been divided into excitation energy slices, taking into account the main peaks and the structures. Background contributions have been subtracted out, as described in Sec. III. The energy slices up to $E_x=10.5$ MeV are displayed in Fig. 3(a).

The lowest l ($3p$ and $2s$) orbitals have not been included in the least-squares fit of the three observable angular distributions, as the expected cross sections are very small. The $2f$ or $2d$ transitions have been considered, as their cross sections at the smallest angles may be comparable to those of $1h_{9/2}$ or $1g_{7/2}$ transitions. As reported in Ref. [13], the reaction at $E_d=200$ MeV allows a very clear identification of j_+ versus j_- levels but not as well of the orbital l value. Transitions to valence levels were considered up to $E_x=6.7$ MeV. Beyond that excitation energy, hole states in the first inner shell were taken into account. These results point out clearly the need of valence and inner hole contributions between $E_x=6.7$ and 10 MeV, which have been included in the final analysis.

Typical angular distribution data and fits are shown in Figs. 4 and 5, for excitation energy slices respectively below and above $E_x=6.7$ MeV. The spectroscopic factors of the two highest l transitions are also indicated.

A. The excitation energy region 0–6.7 MeV

Most angular distributions obtained for the cross sections have rather similar shapes, except for weakly excited groups at $E_x=2.7$, 3.2, and 3.8 MeV [Fig. 3(a)] which have steeper slopes and the group at $E_x=4.2$ MeV which has a smaller slope than all those predicted by the DWBA calculations. Larger differences are observed among the analyzing power angular distributions. While none of them exhibits the characteristic features of a single pickup transition, the negative values of A_y already indicate a dominant contribution of the $1i_{13/2}$ strength in most excitation energy slices.

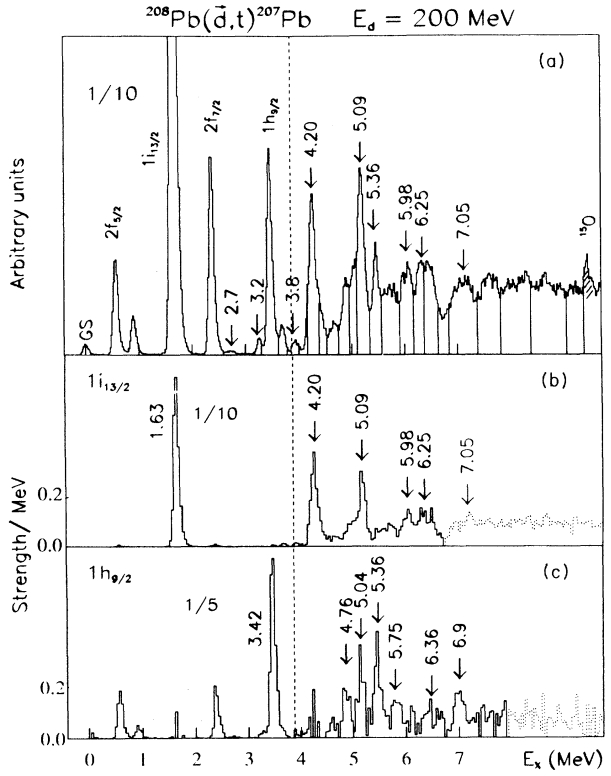

FIG. 3. Groups and structures in the excitation energy spectrum of ^{207}Pb. (a) Excitation energy slices up to $E_x=10.5$ MeV used in the data analysis. (b) Excitation energy spectrum built for the $1i_{13/2}$ strength, as explained in Sec. IV. The histogram dotted part corresponds mainly to the $1h_{11/2}$ strength. (c) The same for the $1h_{9/2}$ strength. The histogram dotted part corresponds to the overlap of the $1h_{9/2}$ and $1g_{7/2}$ strengths.

Systematic attempts were made to achieve the best χ^2 values for each energy slice data. Acceptable fits are generally obtained by taking into account $1i_{13/2}$ and $1h_{9/2}$ levels only. The best fits are however achieved with additional $2f_{7/2}$ levels (or, in two cases, $2f_{5/2}$ or $2d_{3/2}$ levels) in several energy slices. The improvements bear especially on the cross section angular distributions (see Fig. 4). Typical fitting errors on the spectroscopic factors of most of the $1i_{13/2}$ and $1h_{9/2}$ fragments are respectively 8% and 15%. We do not succeed to better reproduce the differential cross section slope of the group at $E_x=4.2$ MeV and the analyzing powers of the group at $E_x=5.99$ MeV.

1. The $1i_{13/2}$ and $1h_{9/2}$ spectroscopic factors

The overall results of the present experiment are compared in Table I (top) with those of Refs. [2–5]. We em-

phasize the following remarks. The spectroscopic factors of the first $1i_{13/2}$ level deduced from our study of the $(\vec{d},t)$ reaction [13] and from Refs. [2–4] agree fairly well. The group at $E_x=4.2$ MeV is here tentatively attributed to the $1i_{13/2}$ strength, in agreement with the previous works. This attribution is questioned later on. The summed spectroscopic factors of the other $1i_{13/2}$ transitions agree rather well with the estimate of Ref. [4] but not with the results of Ref. [3] where only one $1i_{13/2}$ group beyond $E_x=4.2$ MeV was identified.

One notices that all $1h_{9/2}$ spectroscopic factors given in Refs. [2–5] are significantly larger than the results of

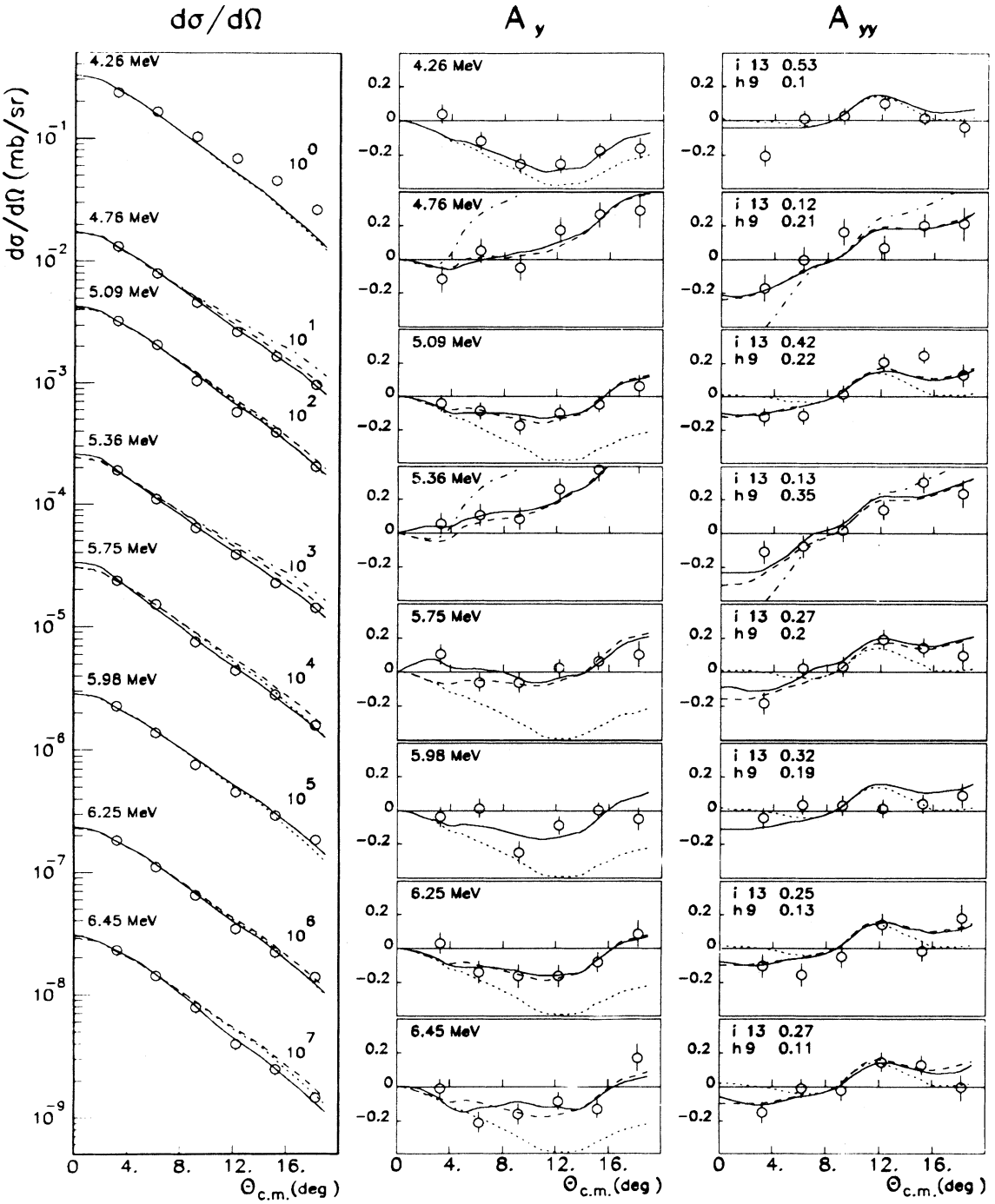

FIG. 4. Angular distributions of the cross sections and analyzing powers for excitation energy slices below $E_x=6.65$ MeV. The peak or mean energy in each slice is indicated in the left and middle parts of the figure. The $1i_{13/2}$ and $1h_{9/2}$ spectroscopic factors, $(i13,h9)$, corresponding to the best angular distribution fits shown as thick solid lines are given in the right part of the figure. Fits obtained with both $1i_{13/2}$ and $1h_{9/2}$ transitions only are shown as dashed lines where they do not correspond to the best fit. Angular distributions of pure transitions are indicated as dotted lines ($1i_{13/2}$) or dash-dotted lines ($1h_{9/2}$).

the present experiment. The relative spectroscopic factors are however in rather good agreement.

2. Excitation energies of the main $1i_{13/2}$ and $1h_{9/2}$ groups: Comparison with previous results

Distributions of the $1i_{13/2}$ and $1h_{9/2}$ strengths have been built from 9° and 12° summed spectra, using Eqs. (1), taking into account mean $2f_{7/2}$ and $2d_{3/2}$ contributions. The suppression of the $1h_{9/2}$ and $2f$ first levels in the resulting $1i_{13/2}$ spectrum shown in Fig. 3(b) indicates that the procedure is very good for the strength which dominates the cross section in the experimental spectra. The $1h_{9/2}$ spectrum Fig. 3(c) exhibits only 16% residual strength of the first $2f_{7/2}$ and $2f_{5/2}$ levels. The attribution of the main peaks observed in Fig. 3(c) beyond $E_x=4.5$ MeV to the $1h_{9/2}$ strength is thus justified.

The energies of the levels located in the $1i_{13/2}$ and $1h_{9/2}$ spectra are compared in Table I (bottom) with those of the levels attributed to these two strengths in Refs. [2–4]. The agreement is fairly good. The main discrepancy is observed around $E_x=5.05$ MeV. We find that this group not resolved in previous experiments and attributed to the $1h_{9/2}$ strength is a doublet $\frac{9}{2}^-$, $\frac{13}{2}^+$, which cross section is dominated by the contribution of the $1i_{13/2}$ level. Other $1i_{13/2}$ levels or complex groups were not at all identified [3] or only attributed to $l=5$ or 6 [4]. Previous attributions of the weak groups at $E_x=3.6$ and 4.72 MeV and 5.62 MeV are not confirmed.

3. The $2f_{7/2}$ and $2d_{3/2}$ contributions

Except for a $d_{3/2}$ (or $2f_{5/2}$) level in the excitation energy slice at $E_x=5.75$ MeV (with $C^2S=0.8\pm0.3$), the $2f$ (or $2d$) contributions deduced from the present analysis correspond fairly well to those expected from the well known $2f_{7/2}$ level at $E_x=4.5$ MeV [20], and the $2f$ levels

TABLE I. Top: $1i_{13/2}$ and $1h_{9/2}$ summed spectroscopic factors. Excitation energy region $E_x=0$–6.7 MeV. Bottom: Excitation energies of the levels or groups attributed $1i_{13/2}$ or $1h_{9/2}$ in the present work and Refs. [2–4]. The levels at 1.63 and 3.42 MeV are omitted.

E_x (MeV)	$(\vec{d},t)$ 200 MeV This work	(p,d) 49 MeV Ref. [2]	$(^3\mathrm{He},\alpha)$ 70 MeV Ref. [3]	$(^3\mathrm{He},\alpha)$ 101 MeV Ref. [4]	$(^3\mathrm{He},\alpha)$ 205 MeV Ref. [5]
		$1i_{13/2}$ spectroscopic factors			
1.63	10.1	8.50	12.0	10.1	10.0[a]
4.2	0.5[b]	0.44	1.16	1.0	0.82
others	2.4	0.19[c]	0.7	2.8[d]	1.5[d]
		$1h_{9/2}$ spectroscopic factors			
3.42	4.05	6.8	6.9	5.0	6.45
others	2.07	0.71[c]	3.6	3.1[d]	4.3[d]

$(\vec{d},t)$ This work		(p,d) Ref. [2]		$(^3\mathrm{He},\alpha)$ Ref. [3]		$(^3\mathrm{He},\alpha)$ Ref. [4]	
$i_{13/2}$	$h_{9/2}$	$i_{13/2}$	$h_{9/2}$	$i_{13/2}$	$h_{9/2}$	$i_{13/2}$	$h_{9/2}$
	(3.2)	3.21					3.25[e]
3.62			3.56		3.66		3.6[e]
4.20[f]		4.22		4.25		4.2[g]	
	4.76	4.76				4.8	
4.9							
	5.04						
5.09			5.08		5.13		5.09
	5.36		5.39		5.41		5.35
5.6					5.62		
	5.75						
5.98				5.99			
6.25							
	6.35						
	6.9						
7.05[f]							

[a]Normalized value.
[b]Upper limit (see Sec. IV C).
[c]Levels up to $E_x=5.5$ MeV only.
[d]Assuming equal contributions of $l=5$ and $l=6$ levels in some excitation energy slices.
[e]Attributed $1h_{9/2}$ or $1i_{11/2}$.
[f]Attributed $1i_{13/2}$ or $1h_{11/2}$ (see Sec. IV C).
[g]Attributed $1i_{13/2}$ or $1j_{15/2}$.

previously identified at $E_x = 4.76$, 5.13, and 6.37 MeV [3] and $E_x = 5.47$ MeV [2].

B. The excitation energy region $E_x = 6.7 - 14.5$ MeV

Background cross sections estimated as described in Sec. III have been subtracted out from the data. Such corrections reach typically 5% and 30% around $E_x = 7$ and 14.5 MeV, respectively (see Fig. 1). The contributions from the low excitation energy tails of the $1g_{9/2}$ and deeper hole state strength distributions (estimated ~5% of the cross section) have also been subtracted.

As shown in Fig. 5, the shapes of the experimental differential cross sections are similar to those obtained for most of the lower excitation energy slices (Fig. 4). Vector analyzing powers have also negative values over most of the angular range, especially for the slices related to the structures between $E_x = 6.65$ and 10 MeV. This confirms unambiguously a dominant contribution of the $1h_{11/2}$ strength.

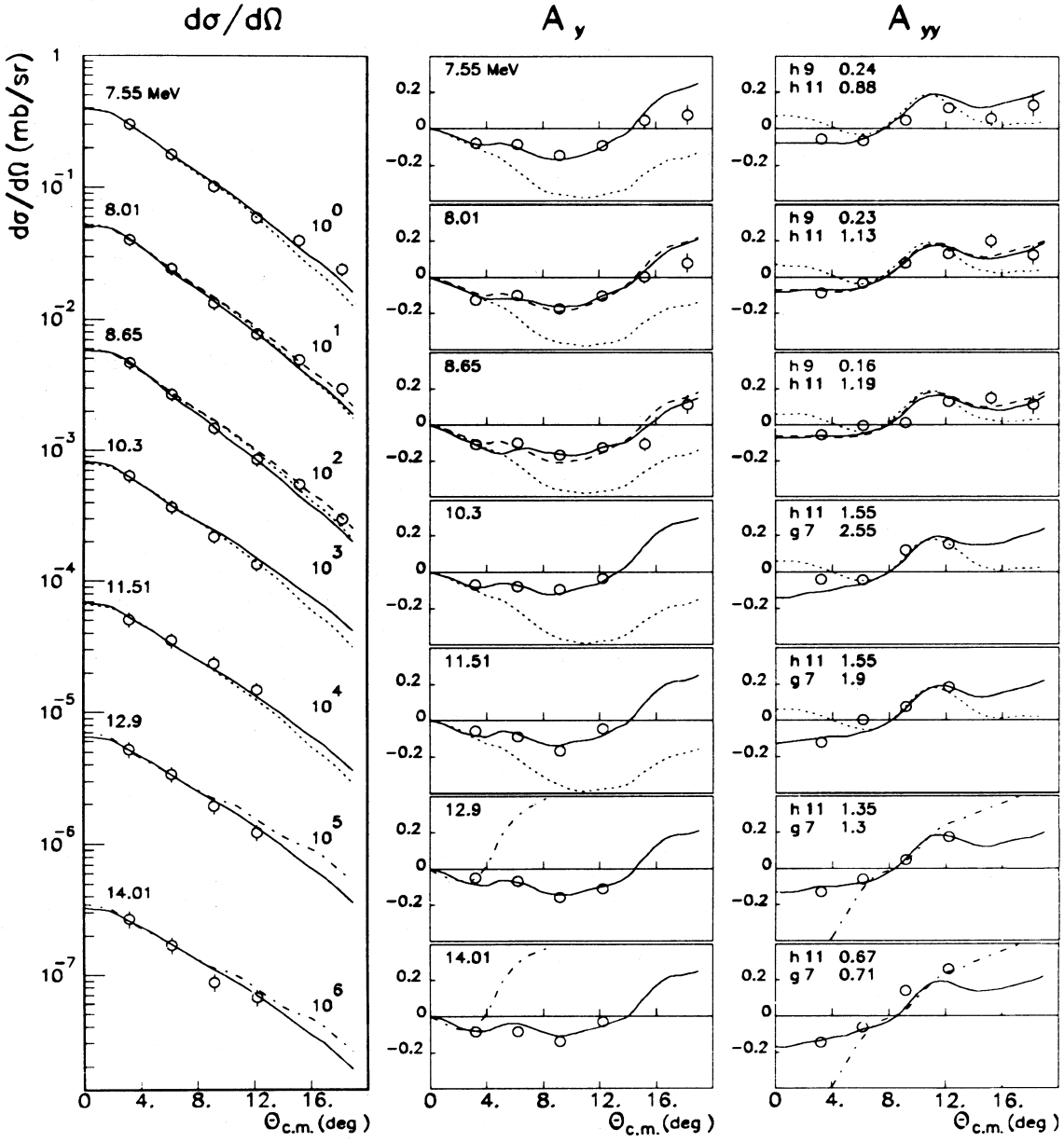

FIG. 5. Angular distributions of cross sections and analyzing powers for excitation energy slices between $E_x = 6.65$ and $E_x = 14.5$ MeV. The background contributions are subtracted. The mean excitation energy of each slice is indicated in the left and middle parts of the figure. The $1h_{11/2}$ and $1h_{9/2}$ or $1g_{7/2}$ spectroscopic factors, ($h11$,$h9$,$g7$), corresponding to the best angular distribution fits shown as thick solid lines are given in the right part of the figure. Fits obtained with both $1h_{11/2}$ and $1h_{9/2}$ (or $1g_{7/2}$) transitions only are shown as dashed lines where they do not correspond to the best fit. Angular distributions of pure transitions are indicated as dotted lines ($1h_{11/2}$) or dash-dotted lines ($1g_{7/2}$).

Least-squares fits of the three observable angular distributions have been systematically performed, assuming several combinations of 2 or 3 transitions in each excitation energy slice such as $1h_{9/2}$ and $1h_{11/2}$ or $1g_{7/2}$ and $1h_{11/2}$ transitions, and also additional $2d_{3/2}$ or $2d_{5/2}$ transitions. It appears necessary to consider contributions of the $1h_{9/2}$ strength as its sum rule is by far not reached by the fragments attributed below $E_x = 6.7$ MeV [see Table I (top)].

The summed spectroscopic factors deduced for the $1h_{11/2}$, $1h_{9/2}$, and $1g_{7/2}$ strengths are summarized in Table II.

The quality of the best fits are illustrated in Fig. 5. Acceptable fits are already achieved without the $2d$ states. A good χ^2 value could not be achieved for the energy slice at $E_x = 7.05$ MeV, mainly due to the too small slope of the cross section angular distribution. The $2d_{5/2}$ cross sections contribute mainly to the first slices, with some 50% or more of the strength concentrated over 2 MeV around $E_x = 8.7$ MeV. It is worthwhile to notice that omitting the $2d$ contributions would give negligible effect on $1h_{11/2}$ spectroscopic factors, while the $1h_{9/2}$ or $1g_{7/2}$ values would decrease by about 15%. The main uncertainties on these last strengths come however from the different assumptions used in the DWBA calculations (as indicated in Table II) and from the background subtraction for the highest excitation energy slices.

In previous works, the $1h_{11/2}$ strength was studied in the region of the bump, up to $E_x = 10.5$ MeV at most. The result obtained for that bump in the present experiment is compared in Table III with those of Refs. [3–6]. The agreement is good [3–5], or fairly good [6], except for the larger C^2S obtained in the second analysis performed in Ref. [3] using the bump centroid energy. It is worthwhile to notice that in the previous works [3–6], no contribution of the $1h_{9/2}$ nor of the $1g_{7/2}$ or $2d$ strengths was taken into account in the above discussed excitation energy range.

In Ref. [3], the location of the $T_< 1g_{7/2}$ strength centroid was indirectly estimated from the position of a narrow peak, further on not confirmed [4], attributed to the $T_>$ strength. On the other hand, a possible broad structure between $E_x = 10$ and 17.5 MeV was tentatively attributed to the $1g_{9/2}$ strength. In Ref. [4], a suggested structure from $E_x = 9.5$ to 20.5 MeV was tentatively attributed to both the $1g_{7/2}$ and $1g_{9/2}$ strengths. As indicated in Refs. [3,4], these features were difficult to separate from a large background. Moreover, their attribution to the $1g$ strengths only are invalidated by the significant $1h_{11/2}$ strength found beyond the main bump in the present experiment. The discussion of Ref. [6] pointed out that the global cross sections obtained in the same region would account for the $1g$ strengths and the missing $1h_{11/2}$ strength. No indication was given on the $1g_{7/2}$ or $1g_{9/2}$ strength locations.

C. Indirect pickup contributions

The analysis based on DWBA calculations takes only into account the one hole component of the residual level wave functions. As discussed later on, the observed strong fragmentation of valence and inner hole states in ^{207}Pb is related to the role of the one-quasiparticle–one-phonon ($1qp \otimes 1ph$) collective configurations present in the corresponding excitation energy range. These configurations also contribute to the level population via indirect pickup. We have made a cursory investigation of such contributions using the code CHUCK [21], with parameter sets ZR given in Table I of Ref. [13]. It has been shown in Ref. [13] that the reference level observables could be successfully described in the framework of the zero range approximation by adjusting the optical potentials. The calculations for a sample of pure collective configurations lead to the following remarks.

The overall behavior of analyzing power angular distributions is in many cases similar to that calculated for direct pickup, for the same spin and parity of the final state, while differential cross sections exhibit significantly smaller slopes. Such feature is only observed for the group at $E_x = 4.2$ MeV. Two-step pickup would thus play a minor role in all other cases.

The largest cross sections are predicted, as expected, for the configurations involving the most collective vibrations, in particular the strong octupole vibration at $E_x = 2.61$ MeV in ^{208}Pb, and the quadrupole vibrations. The summed cross sections for purely collective $\frac{13}{2}^+$ levels would reach some 15% of the cross sections of the $1i_{13/2}$ groups between $E_x = 3$ and 6.7 MeV resulting from the DWBA analysis The corresponding percentages would be smaller for the $\frac{9}{2}^-$ states (about 5%) and similar for $\frac{11}{2}^-$ states.

Two-step and one-step pickup amplitudes can contribute coherently to the population of a same level. It has however been shown that such interference effects would average out over a large excitation energy range including many levels with the same spin and parity. In the

TABLE II. $1h_{11/2}$, $1h_{9/2}$, $1g_{7/2}$ summed spectroscopic factors in the excitation energy range $\Delta E_x = 6.7$–14.5 MeV.

$1h_{11/2}$		$1h_{9/2}$		$1g_{7/2}$	
ΔE_x (MeV)	C^2S	ΔE_x (MeV)	C^2S	ΔE_x (MeV)	C^2S
6.7–14.5	10.6–(9.7)[a]	6.7–10.8[b]	1.1–(1.6)[a]	7.8–14.5[b]	6.7–(5.0)[a]
		6.7–9.0[c]	0.9–(1.2)[a]	9.0–14.5[c]	7.4–(5.5)[a]

[a]With a nonstandard choice for the DWBA analysis and background (see Sec. III).
[b]With a smooth overlap of the $1h_{9/2}$ and $1g_{7/2}$ strengths from $E_x = 7.8$ to 10.8 MeV.
[c]With no overlap of the $1h_{9/2}$ and $1g_{7/2}$ strengths.

TABLE III. Summed spectroscopic factors in the $1h_{11/2}$ bump measured in the excitation energy range ΔE_x (background subtracted).

	This work	Ref. [3]	Ref. [4]	Ref. [5]	Ref. [6]
ΔE_x (MeV)	6.7–9.75	6.7–10.5	6.7–9.75	6.6–9.9	6.6–9.8
C^2S	5.5 (5.1)[a]	5.6 (8.5)[b]	5.23	5.0[c]	6.4

[a]With a nonstandard choice for the DWBA analysis and background (see Sec. III).
[b]C^2S of the whole structure analyzed at the centroid excitation energy.
[c]Background subtracted as reestimated in Ref. [4].

specific case of the 4.2 MeV group, analyses performed with one- and two-step amplitudes indicate that the observable angular distributions could be qualitatively described assuming a $\frac{13}{2}^+$ level (including a $2f_{7/2}\otimes 3^-$ collective component) or preferably a $\frac{11}{2}^-$ level (with a $1i_{13/2}\otimes 3^-$ component). The discussion of this point is beyond the scope of the present paper. In the following section, the half of the group cross section has been attributed to the $1i_{13/2}$ strength. Another estimation would not change significantly the overall results on that strength.

V. COMPARISON OF EXPERIMENTAL AND THEORETICAL STRENGTH DISTRIBUTIONS

The spreading mechanism of single particle modes has been a subject of theoretical interest for many years. Important features are now qualitatively understood [22]. In particular, it has been shown that the coupling of these modes to the core excitations is responsible both for the level compression around the Fermi surface and for major aspects of the strength fragmentation.

The coupling of the single particle degrees of freedom to the surface modes is generally treated via microscopic calculations, starting with the description of nucleon motion in some average potential. This is the case, in particular, for the many calculations performed in the framework of the quasiparticle-phonon coupling model (QPM) which have recently been surveyed and compared with the available experimental data [23]. In a recent phenomenological approach based on dispersion relations, the overall effects of the coupling are considered. Spectral functions are calculated in a modified mean field [24].

The nucleus ^{207}Pb, with one neutron hole in the doubly magic core has been considered as a test case for the different theoretical approaches [19,24–29].

Bortignon *et al.* [25] and Van Giai *et al.* [28] use the Skyrme III interaction to calculate Hartree-Fock single particle wave functions and energies. A surface effective interaction with the radial shape given by the derivative of a Woods-Saxon potential is used in Ref. [25] both to calculate the core excitations within the random phase approximation (RPA) and to describe the particle-vibration coupling. A self-consistent RPA calculation is performed in Ref. [28] and the coupling interaction between the quasiparticle and the core excitation is also derived from the Skyrme III force. Low lying states of natural parity and giant resonances of the core are taken into account in both calculations.

The valence and inner hole fragmentation in ^{207}Pb is calculated by Soloviev *et al.* [26] in the framework of the QPM. The phonon excitations of ^{208}Pb are generated by separable multipole and spin-multipole forces and the main ^{208}Pb collective levels are fitted within the RPA. The coupling of neutron holes with a large number of 1qp⊗1ph and 1qp⊗2ph states is taken into account. The more complete results recently obtained in the same framework by Vdovin [27] are used in the comparison with the present experimental data. Improvements are introduced on the adopted particle spectrum and on the radial form factor shape of the separable force. Additional hole states are calculated.

Mahaux *et al.* [19,24] have developed extrapolation procedures to derive the modified mean field of ^{208}Pb at negative energy, starting from optical potential measured for low incident energy neutrons. The energies and strengths of the valence quasihole levels are predicted. Spectral functions are given for the $1h_{11/2}$ inner hole state [19,24] and for the $1g_{7/2}$ and $1g_{9/2}$ deeper states [19].

In Tables IV and V, we summarize the characteristics deduced from the present experiment for the ^{207}Pb valence and inner hole states, respectively, together with the results deduced from the calculations of Refs. [19,24,25,27,28]. The experimental and theoretical strength distributions are compared in Figs. 6,7 and Figs. 8,9.

A. The $1i_{13/2}$ and $1h_{9/2}$ valence strengths

In the case of the valence states, the strengths are shared between one main fragment, the quasihole level, and the many other fragments, each of them exhausting a small spectroscopic strength. The main characteristics of interest for these last fragments are their summed strength, the centroid excitation energy, and the width, here calculated in the Gaussian approximation. The experimental and theoretical results are compared in the upper and lower parts, respectively, of Table IV, for the $1i_{13/2}$ and $1h_{9/2}$ states. The calculations of Refs. [25,28] based on the nonlocal Hartree-Fock field are not expected to predict the right absolute excitation energies. The theoretical energy scales have thus been shifted in order to match the experimental positions of the $1i_{13/2}$ and $1h_{9/2}$ quasihole levels. These energies are rather well reproduced in Refs. [19,24,27].

The data analysis induces rather small uncertainties on the $1i_{13/2}$ strength [Table IV (top), Fig. 6(a)]. An in-

correct estimation of that strength in the collective group at $E_x = 4.2$ MeV or small missing fragments not separated from the $1h_{11/2}$ bump would not change significantly the results. The uncertainties on the experimental $1h_{9/2}$ strength [Table IV (bottom), Fig. 7(a)], are somewhat larger, partly due to the analysis and partly to the overlap with the $1g_{7/2}$ strength.

The $1i_{13/2}$ quasihole strength is generally well predicted, except for the too large strength given in Ref. [27]. The summed strength of all other fragments is only reproduced in Ref. [28], the calculated width being however too large. The $1h_{9/2}$ quasihole strength is overestimated in all calculations, except in Ref. [28], while the other fragment summed strength is underestimated in [27] and overestimated in [28]. The strength, centroid, and width of the fragments below $E_x = 6.7$ MeV are somewhat better described in [25,27] than in [28].

The comparison of the experimental strength distributions with the predictions of Refs. [27,28], shown in Figs. 6 and 7, suggests the following remarks.

The positions of the $1i_{13/2}$ groups predicted in Refs. [27,28] beyond $E_x = 5.5$ MeV are fairly similar, while the location of the lower lying group strongly differs. The strength distribution from [28] may be qualitatively compared with the data. One would expect that the two lower lying groups correspond to the experimental groups below $E_x = 5.5$ MeV and the higher lying ones to the structure around $E_x = 6.2$ MeV.

The experimental $1h_{9/2}$ groups between $E_x = 4.76$ and 5.36 MeV may correspond to the levels at 4.4 and 5.2 MeV of Ref. [28] and the structure around $E_x = 6.2$ MeV would be explained (with additional spreading) by the two theoretical levels around $E_x = 6.5$ MeV. The long tail of the experimental distribution toward high excitation energies is only predicted in Ref. [27], but not its absolute strength.

The main discrepancy of the data with the predictions of Ref. [27] bears on the sharing of the strength between the quasihole levels and the other fragments. This feature is fairly well described in Ref. [28]. The smaller number of configurations used in these last calculations may be partly responsible for insufficient spreading, in particular of the $1h_{9/2}$ strength at high excitation energies.

TABLE IV. Top: Integral characteristics of the $1i_{13/2}$ strength distribution. E_x^{max}, $\overline{E_xF}$, Γ_G are the maximum and centroid excitation energy of the fragments and their Gaussian width. $\overline{E_x}$ is the total strength centroid. Bottom: integral characteristics of the $1h_{9/2}$ strength distribution. E_x^{max}, $\overline{E_xF}$, Γ_G, $\overline{E_x}$ as in the upper part.

	Quasihole level		Others fragments					Total
	E_x^{gh} (MeV)	$C^2S/2j+1$	E_x^{max} (MeV)	$\overline{E_xF}$ (MeV)	$C^2S/2j+1$	Γ_G (MeV)	$\overline{E_x}$ (MeV)	$C^2S/2j+1$
This work[a]	1.63	0.72	7.3	5.4	0.19	1.9	2.4	0.91
			7.3	(5.4)	(0.21)	(1.9)	(2.4)	(0.93)
Theory[b]								
Ref. [25]	−0.27[c]	0.78	[6.3]	[4.3]	0.04		[1.8]	0.82
Ref. [27]	1.5	0.91	7.3	5.3	0.07	1.9	1.8	0.98
			10	6.1	0.09	3.5	1.9	1.0
Ref. [28]	−1.32[c]	0.64	[7.3]	[5.2]	0.20	3.5	[2.3]	0.84
			[8.2]	[5.5]	0.22	3.8	[2.4]	0.86
Ref. [19]	1.26	0.71						
Ref. [24]	1.33	0.66						
This work[d]	3.42	0.41	6.7	5.3	0.21	1.93		0.62
			6.7	(5.6)	(0.24)	(2.05)		(0.65)
			10.8	6.3	0.33	3.9	4.7	0.74
			10.8	(6.7)	(0.40)	(3.9)	(5.0)	(0.81)
Theory[e]								
Ref. [25]	−0.58[c]	0.60	[6.0]	[4.9]	0.24		[3.8]	(0.84)
Ref. [27]	3.1	0.76	6.7	4.9	0.14	1.65	3.4	0.90
			10.8	5.9	0.20	4.3	3.7	0.96
Ref. [28]	−1.58[c]	0.43	[7.2]	[4.5]	0.43	3.2	[4.0]	0.86
Ref. [19]	3.1	0.77						
Ref. [24]	3.2	0.7						

[a]Assuming a smooth overlap with the $1h_{11/2}$ strength from $E_x = 6.3$ to 7.3 MeV and taking into account half the 4.2 MeV group cross section. The values within ( ) are derived from the DWBA analysis independent of excitation energy (see Sec. III).

[b]The theoretical energies written with [ ] are obtained by shifting the energy scale to match the first $1i_{13/2}$ level to the experimental position.

[c]Shift of the theoretical energy scale.

[d]Assuming a smooth overlap with $1g_{7/2}$ strength from $E_x = 7.8$ to 10.8 MeV. The values within ( ) are derived from the DWBA analysis independent of excitation energy (see Sec. III).

[e]The theoretical energies written with [ ] are obtained by shifting the energy scale to match the 3.42 MeV level position.

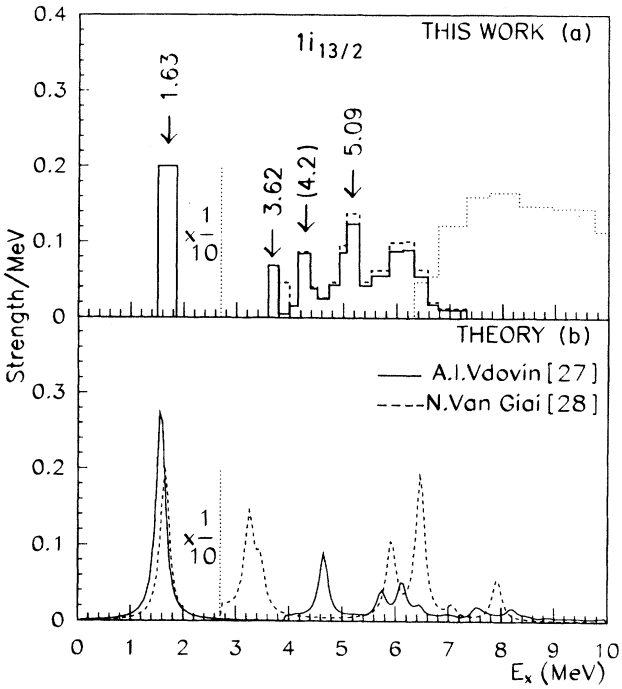

FIG. 6. Experimental and theoretical $1i_{13/2}$ neutron hole strength distributions. (a) Solid line: histogram of the experimental strength (dashed line: with DWBA cross sections independent of E_x). The histogram of the slightly overlapping $1h_{11/2}$ strength is indicated by dotted lines. The strength at $E_x = 4.2$ MeV takes into account the discussion of Sec. IV C. (b) Solid line: results of [27]. Dashed line: results adapted from [28], using for each fragment a Lorentzian distribution with the same smearing parameter (0.2 MeV) as in [27]. The theoretical excitation energy scale has been shifted down by 1.32 MeV.

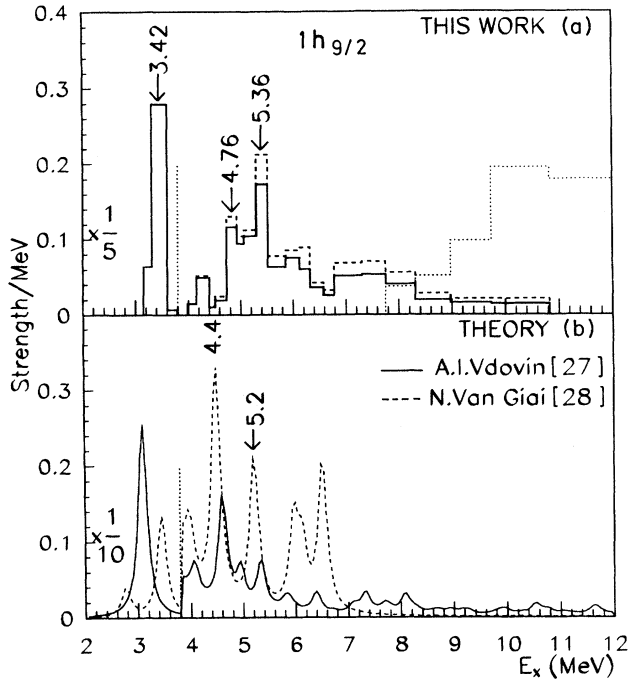

FIG. 7. Experimental and theoretical $1h_{9/2}$ neutron hole strength distributions. (a) Same as Fig. 6(a) but for the $1h_{9/2}$ strength (and the $1g_{7/2}$ strength). (b) Same as Fig. 6(b). The theoretical energy scale of [28] has been shifted down by 1.58 MeV.

B. The $1h_{11/2}$ and $1g_{7/2}$ inner hole strengths

The $1h_{11/2}$ and $1g_{7/2}$ experimental strength distributions are compared with the theoretical predictions of Refs. [19,24,27,28] in Figs. 8 and 9, respectively. The experimental strengths, as expected for single hole states at high excitation energy, are distributed among many unresolved levels. Their important characteristics, i.e., the summed strength, the centroid, and the Gaussian width in each relevant excitation energy interval, the location of the strength distribution maximum, and the spreading width are summarized in Table V.

1. The $1h_{11/2}$ strength

As shown in Fig. 8(c), the microscopic calculations performed with (1qp⊗1ph) components [27,28] already predict that the $1h_{11/2}$ strength is fragmented over more than 10 MeV. In particular, a small fragment is pushed down to very low excitation energy. If identified with the experimental group at $E_x = 4.2$ MeV, the predicted strong collectivity at that level would explain the special behavior of the differential cross sections, as indicated in Sec. IV C. The theoretical strength distributions exhibit two well pronounced peaks in contradiction with the data. Nevertheless, the summed strength, centroid, and Gaussian width from Ref. [28] are in fair agreement with the data for each relevant excitation energy range, as shown in Table V (top).

The two peaks predicted by the (1qp⊗1ph) calculation of Ref. [27] merge into one main peak when (1qp⊗2ph) components are included [see Fig. 8(b)]. Except for weak structures, the calculated strength distribution can be fairly well fitted by a Lorentzian curve. The location of the experimental strength distribution maximum is rather well reproduced, but neither the maximum strength per MeV nor the wide and dissymmetric shape of the experimental strength. The spreading width is much too small [Table V (top)]. A smaller number of (1qp⊗1ph) model states is used in the (1qp⊗2ph) type calculation than in the (1qp⊗1ph) one, and coupling matrix elements lower than 15% of the larger one are dropped. These technical limitations are considered to be partly responsible for the discrepancies observed with the data. The smearing parameter set to 0.5 MeV over the whole excitation energy range is not able to simulate these missing contributions and those of higher order configurations. On the other hand, the discrepancies, also noticed for the valence states, may also originate from the schematic forces used in the model. More precisely, the single particle matrix elements of the radial form factors of the forces would give too small coupling.

The spectral functions calculated in Ref. [19], and in Ref. [24] [see Fig. 8(b)], have Lorentzian-type shapes,

with the width $\Gamma(h_{11/2},E_x)$ increasing with excitation energy, a feature even more striking in the data. The predicted widths are much larger than found by the QPM, but however not large enough on the high excitation energy side. As shown in Table V (top), the centroid energies and the summed strengths given in Refs. [19,24] are fairly consistent with the data while the quasihole energies are somewhat too high.

The experimental results are best reproduced using a Gaussian-type parametrization [see curve *G* in Fig. 8(a) and Table V (top)], as previously used for proton deep hole strength distributions [24]. It is worthwhile to notice that the deduced dependence of the width $\Gamma(1h_{11/2},E_x)$ on the excitation or separation energy (Ref. [24], Eq. 7.35), is larger than the prediction deduced from the dispersive correction to the mean field.

The above discussion concerns the $T_<$ part of the $1h_{11/2}$ strength. Admitting the $T_>$ strength to be concentrated in the known level at $E_x=20.6$ MeV, the experimental isospin splitting amounts to 10.7 MeV. This value, smaller than previous estimations [3,4], is in somewhat better agreement with the value of 9 MeV calculated in Ref. [4] in the framework of Lane's coupled equations [30].

2. *The $1g_{7/2}$ strength*

A large part of the $1g_{7/2}$ inner hole strength and its maximum are identified for the first time in the present experiment. In spite of significant uncertainties and limitations on the studied excitation energy range, the comparison of the present data with the calculations of Refs. [27] and [19] [see Fig. 9 and Table V (bottom)] justifies the following observations.

The experimental summed strength is in fair agreement with both theoretical predictions. The location of the quasihole peak and the strength centroid are also rather well predicted in Ref. [27] while the quasihole peak of Ref. [19] is at least 1 MeV too high. The Lorentzian-type shape of Ref. [19] gives too much strength in the low and high excitation energy tails. A Gaussian-type parametrization achieves a better fit to the present data [see

TABLE V. Top: Integral characteristics of the $1h_{11/2}$ strength distribution. $\bar{E}_x^{\min}$, $E_x^{\max}$ are the excitation energy range limits. $\bar{E}_x$, Γ_G, E_x (peak), and $\Gamma_\downarrow$ are the centroid excitation energy, the Gaussian width, the peak or maximum strength positions, and the spreading width. Bottom: Integral characteristics of the $1g_{7/2}$ strength distribution. See the upper part.

	$E_x^{\min}$ (MeV)	$E_x^{\max}$ (MeV)	$C^2S/2j+1$	$\bar{E}_x$ (MeV)	Γ_G (MeV)	E_x (peak) (MeV)	$\Gamma_\downarrow$ (MeV)
This work[a]	6.3	14.5	0.88 (0.80)	9.9 (9.9)	5.0	8.2[b]	4.5[b]
	6.3	11.9	0.69 (0.64)	9.0 (9.0)	3.4	8.2[b]	{5.3}[b]
	6.7	9.7	0.47 (0.43)	8.2	2.1	8.2[b]	
Theory[c]							
Ref. [25]	[5.2]	[8.6]	0.3	[7.2]	1.5	[7.3,10.3]	
Ref. [27]	6.3	14.5	0.80	8.7	4.2	7.8	1.6[d]
	6.3	11.9	0.71	8.3	2.8		
	6.7	9.7	0.6	7.9	1.7		
Ref. [28]	[6.3]	[11.9]	0.60	[8.9]	2.9	[17.3,9.3]	
	[6.7]	[9.7]	0.45	[8.6]	2.2		
Ref. [19]	6.3	14.5	0.72	9.7	4.3	9.02	3.7
	6.7	9.7	0.39	8.5	1.9		
Ref. [24]	6.3	14.5	0.67	9.7	4.6	8.85	4.5[e]
	6.7	9.7	0.35	8.4	1.9	8.85	{5.4}[f]
This work[g]	7.8	14.5	0.78	11.4	3.7	11[b]	4.5[b]
	7.8	14.5	(0.6)	(11.7)	3.6	11[b]	{4.9}[b]
Theory							
Ref. [27][h]	7.8	14.5	0.81	11.1	2.9	11[b]	1.9[i]
Ref. [19]	7.8	14.5	0.65	12	3.6	12.6	3.4

[a]Assuming a smooth overlap with the $1i_{13/2}$ strength from $E_x=6.3$ to 7.3 MeV. The values with ( ) are deduced with a nonstandard choice for the DWBA analysis and background (see Sec. III).

[b]Quasihole position, spreading width, and full width at half maximum { } corresponding to the Gaussian-type fit shown in Figs. 8(a) and 9(a), curve *G*.

[c]The theoretical energies within [ ] are shifted by -1.4 MeV [25] and by -2.3 MeV for Ref. [28]. The results of Ref. [27] are those with 1qp-2ph components.

[d]From the Lorentzian fit shown in Fig. 8(b).

[e]See Fig. 8(b).

[f]Full width at half maximum with an additional smearing parameter $\Delta=0.5$ MeV (Ref. [24], Eq. 7.19).

[g]Assuming a smooth overlap with the $1h_{9/2}$ strength from $E_x=7.8$ to 10.8 MeV. For the values given within ( ) see footnote (a).

[h]The theoretical values are obtained with 1qp-2ph components.

[i]From the Lorentzian fit shown in Fig. 9(b).

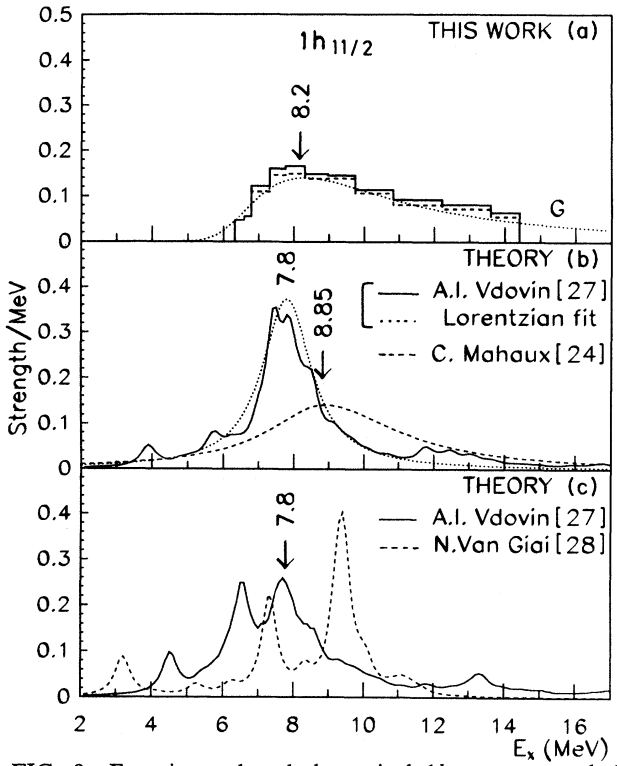

FIG. 8. Experimental and theoretical $1h_{11/2}$ neutron hole strength distributions. (a) The experimental strength is represented by the solid line. The dashed line illustrated typical differences resulting from a nonstandard choice for the DWBA analysis and background as described in Sec. III. The dotted line G is a Gaussian-type fit of the data [see Table V (top)]. (b) Solid line: QPM calculation with (1qp⊗2ph) components [27]. Dotted line: fit of these results by a Lorentzian shape. Dashed line: results of [24]. (c) Solid line: QPM calculation with (1qp⊗1ph) components only. Dashed line: results adapted from [28] as in Fig. 6(b), with the smearing parameter of 0.5 MeV used in [27]. The shift chosen for the theoretical energy scale is −2.3 MeV.

curve G Fig. 9(a) and Table V (bottom)]. The deduced spreading width is larger than predicted in Refs. [19,27].

C. The $1h_{9/2}$-$1h_{11/2}$ spin-orbit splitting

The experimental results on the $1h_{9/2}$ and $1h_{11/2}$ strength distributions give information on the $l=5$ spin-orbit splitting for the first time. The data on the quasihole peaks, the strength centroids, and the deduced spin-orbit splitting are summarized in Table VI together with theoretical predictions.

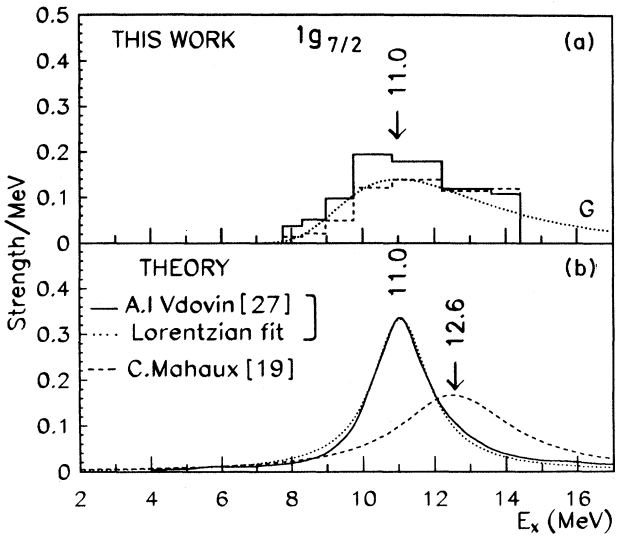

FIG. 9. Experimental and theoretical $1g_{7/2}$ neutron hole strength distributions. (a) Same as Fig. 8(a) but for the $1g_{7/2}$ strength. (b) Solid line: QPM calculation with (1qp⊗2ph) components and a smearing parameter of 1 MeV [27]. Dotted line: fit of these results by a Lorentzian shape. Dashed line: results from [19].

The experimental spin-orbit splitting $\Delta\varepsilon$ is best reproduced in Ref. [27], an agreement to be attributed to the parameters of the Woods-Saxon potential used. The $\Delta\varepsilon$ deduced from the experimental centroids is somewhat smaller than the Hartree-Fock predictions calculated with a Skyrme III force [18] and that deduced from Ref. [28] with significant cutoff of the $1h_{11/2}$ strength [see Table V (top)]. The $\Delta\varepsilon$ values deduced from Refs. [19,24] are significantly larger, a result related to the optical model spin-orbit potential included in the nonmodified mean field, as quoted in Ref. [19]. On the other hand, the spin-orbit spitting $\Delta\varepsilon=4.1$ MeV, calculated by Sheerbaum [31] using nucleon-nucleon realistic forces, but only for the spin saturated core, is somewhat smaller than the experimental finding and the other theoretical predictions.

TABLE VI. $1h_{9/2}$ and $1h_{11/2}$ separation energies ε_{sep} and $l=5$ spin-orbit splitting $\Delta\varepsilon$.

	Quasihole			Centroid		
	ε_{sep} (MeV)		$\Delta\varepsilon$	ε_{sep} (MeV)		$\Delta\varepsilon$
	$1h_{9/2}$	$1h_{11/2}$	(MeV)	$1h_{9/2}$	$1h_{11/2}$	(MeV)
This work	10.8[a]	15.6	4.8	12.1	17.3	5.2
Theory						
Ref. [18]				12.6	18.2	5.6
Ref. [19]	10.4	16.3	5.9	10.4	17.0	6.6
Ref. [24]	10.6	16.1	5.6	10.6	17.6	7.0
Ref. [27]	10.4	15.1	4.5	11.0	16.0	5.0
Ref. [28]	12			12.9	18.5	5.6

[a]Reference [20].

VI. SUMMARY AND CONCLUSIONS

We have studied the highly excited neutron hole states in ^{207}Pb, by means of the $(\vec{d},t)$ reaction at $E_d=200$ MeV. Differential cross sections, and vector and tensor analyzing powers, have been measured for the first time, allowing spin determination of the highest j valence and inner hole states up to $E_x=14.5$ MeV.

The clear characteristics of the analyzing power angular distributions of j_+ versus j_- states have allowed an unambiguous j assignment to the main valence groups while the previous experimental results relied only on l identification.

The groups that attributed $1i_{13/2}$ beyond the first level and achieve about 20% of the sum rule, confirming a rather large fragmentation of that strength. The $1h_{9/2}$ valence strength is nearly equally shared between the quasihole level and the other fragments. A significant spreading of that strength beyond $E_x=6.7$ MeV is found in the present experiment.

The bump centered around $E_x=8.2$ MeV was previously attributed to the $1h_{11/2}$ strength [3–6]. The present results unambiguously confirm the dominant contribution of that strength; however, other contributions to this bump are not negligible. The measurement of the three observables σ, A_y, and A_{yy} has allowed a determination of the $1h_{11/2}$ strength beyond the bump, achieving $\sim$85% of the sum rule, and has given the first direct evidence for the $1g_{7/2}$ deep hole strength.

An important consequence of the localization of the major part of both the $1h_{9/2}$ and $1h_{11/2}$ strengths is the determination of the spin-orbit splitting of those $l=5$ orbitals in the doubly magic nucleus ^{208}Pb.

The $1i_{13/2}$, $1h_{9/2}$, $1h_{11/2}$, and $1g_{7/2}$ experimental strength distributions have been compared with theoretical predictions.

The Dubna group has been rather successful in reproducing qualitatively, within the QPM, many features of highly excited hole or particle states in open shell nuclei [23]. In the present case, the predictions of Vdovin [27] fail to reproduce several features of the data, in particular, the sharing of the $1i_{13/2}$ and $1h_{9/2}$ valence strengths between the quasihole level and the other fragments. These deficiencies might be attributed to the too small coupling interaction. Even if the large phonon basis and (1qp$\otimes$2ph) components explain qualitatively significant features of the inner hole strength distributions, additional spreading is clearly needed.

The self-consistent calculations of Van Giai [28] using a coupling interaction derived from the Skyrme III force reproduce better the qualitative features of the $1i_{13/2}$ and $1h_{9/2}$ valence strengths. The cutoff on highly excited configurations and the intrinsic limitations due to the (1qp$\otimes$1ph) approximation are responsible for pronounced structures in the calculated $1h_{11/2}$ strength distribution, in contradiction with the experiment.

The calculations by Mahaux and Sartor [19,24] in a modified mean field predict the peaking of the $1h_{11/2}$ strength and especially of the $1g_{7/2}$ strength at too high excitation energies. The large widths of the experimental strengths are better reproduced than in Refs. [27,28]. The Gaussian-type parametrizations of the data, following Ref. [24], indicate a larger dependence of the inner hole widths with excitation energy than predicted by the modified mean field calculations.

Van Neck *et al.* [32] have recently shown that the description of proton deep hole states could be significantly improved including higher order term corrections to the mean field. It would be interesting to use this approach in the case of neutron hole states. Further theoretical efforts are also needed for an improved description of pick up reactions populating highly excited states, taking into account their many collective components.

ACKNOWLEDGMENTS

We would like to thank C. Mahaux, N. Van Giai, and A. I. Vdovin for helpful discussions or comments. We are indebted to N. Van Giai and A. I. Vdovin for communication of their detailed results. We thank J. C. Duchazeaubeneix and J. C. Lugol for their help during the experiment and the technical staff of the Laboratoire National Saturne for its efficient assistance.

[1] W. A. Lanford, Phys. Rev. C **11**, 815 (1975).
[2] S. M. Smith, P. G. Roos, C. Mozaed, and A. M. Bernstein, Nucl. Phys. **A173**, 32 (1971).
[3] S. Galès, G. M. Crawley, D. Weber, and B. Zwieglinsky, Phys. Rev. C **18**, 2475 (1978).
[4] J. Guillot, J. Van de Wiele, H. Langevin-Joliot, E. Gerlic, J. P. Didelez, G. Duhamel, G. Perrin, M. Buenerd, and J. Chauvin, Phys. Rev. C **21**, 879 (1980).
[5] E. Gerlic, J. Källne, H. Langevin-Joliot, J. Van de Wiele, and G. Duhamel, Phys. Lett. **57B**, 338 (1975); J. Van de Wiele, E. Gerlic, H. Langevin-Joliot, and G. Duhamel, Nucl. Phys. **A297**, 61 (1978).
[6] H. Langevin-Joliot, E. Gerlic, J. Guillot, M. Sakai, J. Van de Wiele, A. Devaux, P. Force, and G. Landaud, Phys. Lett. **114B**, 103 (1982).
[7] B. Meyer, H. E. Conzett, W. Dahme, D. G. Kovar, R. M. Larimer, and Ch. Leemann, Phys. Rev. Lett. **32**, 1452 (1974).
[8] L. D. Knutson, B. P. Hichwa, A. Barroso, A. M. Eiro, F. D. Santos, and R. C. Johnson, Phys. Rev. Lett. **35**, 1570 (1975).
[9] L. D. Knutson, P. C. Colby, and B. P. Hichwa, Phys. Rev. C **24**, 411 (1981).
[10] Y. Toba, K. Nagano, Y. Aoki, S. Kunori, and K. Yagi, Nucl. Phys. **A359**, 76 (1981).
[11] J. J. Kraushaar, J. R. Shepard, D. W. Miller, W. W. Jacobs, W. P. Jones, and D. W. Devins, Nucl. Phys. **A394**, 118 (1983).
[12] H. Nann, D. W. Miller, W. W. Jacobs, D. W. Devins, W. P. Jones, and Li Quing-Li, Phys. Rev. C **27**, 1073 (1983).
[13] J. Van de Wiele, H. Langevin-Joliot, J. Guillot, L. H. Rosier, A. Willis, M. Morlet, G. Duhamel-Chrétien, E. Gerlic, E. Tomasi-Gustafsson, N. Blasi, S. Micheletti, and S. van der Werf, Phys. Rev. C **46**, 1863 (1992).

[14] S. Galès, G. M. Crawley, D. Weber, and B. Zwieglinsky, Phys. Rev. Lett. **41**, 292 (1978).
[15] G. Duhamel, G. Perrin, J. Chauvin, M. Buenerd, E. Gerlic, J. Guillot, J. P. Didelez, H. Langevin-Joliot, and J. Van de Wiele, Phys. Lett. **78B**, 213 (1978).
[16] N. Austern, Nucl. Phys. **A292**, 190 (1977); W. D. M. Rae, Ph.D. thesis, Oxford, 1976 (unpublished).
[17] C. Kalbach, Phys. Rev. C **37**, 2350 (1988), and references therein.
[18] M. Beiner, H. Flocard, and Nguyen Van Giai, Nucl. Phys. **A238**, 29 (1975).
[19] C. Mahaux and R. Sartor, Nucl. Phys. **A493**, 157 (1989).
[20] M. R. Schmorak, Nucl. Data Sheets **43**, 383 (1984).
[21] Program CHUCK, P. D. Kuntz, University of Colorado (unpublished).
[22] G. F. Bertsch, P. F. Bortignon, and R. A. Broglia, Rev. Mod. Phys. **55**, 287 (1983), and references therein.
[23] S. Galès, Ch. Stoyanov, and A. I. Vdovin, Phys. Rep. **166**, 125 (1988), and references therein.
[24] C. Mahaux and R. Sartor, Adv. Nucl. Phys. **20**, 1 (1991), and references therein.
[25] P. F. Bortignon and R. A. Broglia, Nucl. Phys. **A371**, 405 (1981).
[26] V. J. Soloviev, Ch. Stoyanov, and V. V. Voronov, Nucl. Phys. **A399**, 141 (1982).
[27] A. I. Vdovin, private communication (1992).
[28] Nguyen Van Giai, in Proceedings of the International Symposium on Highly Excited States in Nuclear Reactions, Osaka, Japan, 1980, edited by H. Ikegami (RCNP, Osaka, Japan), p. 682; and private communication (1992).
[29] R. Majumdar, J. Phys. G **13**, 1429 (1987).
[30] A. M. Lane, in *Isospin in Nuclear Physics,* edited by D. H. Wilkinson (North-Holland, Amsterdam, 1969), p. 511.
[31] R. Scheerbaum, Nucl. Phys. **A257**, 77 (1976).
[32] D. Van Neck, M. Waroquier, and J. Ryckebush, Nucl. Phys. **A530**, 347 (1991); D. Van Neck, M. Waroquier, V. Van der Sluys, and K. Heyde, Gent Institute for Nuclear Physics report (1992).